Extrapolation of the dispersive optical model to the resonance region for neutrons on ^{86}Kr

C. H. Johnson
Oak Ridge National Laboratory, Oak Ridge, Tennessee 37831

R. F. Carlton
Middle Tennessee State University, Murfreesboro, Tennessee 37132

R. R. Winters
Denison University, Granville, Ohio 43023

(Received 26 September 1988)

The neutron-^{86}Kr mean field is formulated in terms of a dispersive optical model potential in which the real part contains dispersive contributions derived from the imaginary part by the dispersion relation. The dispersive contribution is added to the Hartree-Fock potential, which is assumed to have a Woods-Saxon shape and a depth that decreases linearly with increasing energy. The shape parameters for all components of the potential are assumed to be independent of energy. The model is formulated in terms of the energy relative to the Fermi energy, and the imaginary potential is assumed to be symmetric about the Fermi energy, which is set equal to -7.7 MeV on the basis of the empirical level structure for n-^{86}Kr. All other parameters are taken from earlier analyses of other nuclei, particularly of ^{89}Y. The model is shown to give good overall predictions for the n-^{86}Kr mean field by comparison to the following three sets of empirical data: (i) the observed energies of the occupied and unoccupied valence levels, (ii) the energy-averaged total cross section for neutron energies up to 25 MeV, and (iii) the averaged scattering functions for s-, p-, and d-wave neutrons in the resolved resonance region from 0.015 to 0.96 MeV. The latter comparison is the unique feature of this work; the partial-wave-scattering functions that are available for s, p, and d waves in the resonance region for ^{86}Kr make possible detailed comparisons to the scattering functions from the model.

I. INTRODUCTION

The neutron-nucleus interaction is described approximately by a complex mean field whose central part is local;

$$\mathcal{M}(r;E)=\mathcal{V}(r;E)+i\mathcal{W}(r;E)\ . \tag{1.1}$$

In addition, there is a spin-orbit component. The mean field varies smoothly as the neutron energy E changes sign; for positive energies, it is called the optical model potential (OMP) and, for negative energies, its real part is the shell model potential. The energy dependence of $\mathcal{M}(r;E)$ is quite complicated in the region near the Fermi energy, which separates the occupied and unoccupied single-particle states at negative energies, and this complicated behavior is described in terms of the dispersion relation[1] (DR), which connects a part of the real component of the potential to the imaginary component.

Recent analyses[2–7] for the doubly closed-shell nuclei ^{40}Ca and ^{208}Pb have shown that the introduction of the dispersive component into the neutron mean field results in a good description of the empirical data over a very broad region, including both negative and positive energies, even though there are few adjustable parameters in the model. For negative energies, predictions were made not only of the single-particle energies but also other bound state properties, such as occupation numbers, absolute spectroscopic factors and rms radii. Those studies involved two alternative methods, the "iterative-moment" analysis[2–5] and the "dispersive optical model" analysis.[6,7] For the moment method, one begins with OMP parameters that have been obtained at positive energies by conventional multiparameter OMP analyses of scattering data and, using ratios of various radial moments, deduces the mean field for a broad region of both positive and negative energies. In contrast, the dispersive optical model analysis incorporates the dispersion relation into the original fitting of the data. The iterative-moment analysis was used[2–5] for both proton and neutron fields for ^{40}Ca and for ^{208}Pb, whereas the dispersive optical model analyses were only for the neutron fields.

The striking success of these models for the doubly closed-shell nuclei ^{40}Ca and ^{208}Pb leads one to expect similar success for other nuclei. Good candidates are the nuclei near $A=90$ which have 50-neutron closed shells; these are ^{86}Kr, ^{87}Rb, ^{88}Sr, and ^{89}Y, ^{90}Zr, and ^{92}Mo. In fact, Mahaux and Sartor[8] used the iterative-moment approach to deduce the n-^{89}Y mean field and, quite recently, Delaroche *et al.*[9] made a dispersive OMP analysis for the n-^{90}Zr mean field. The present predictions for n-^{86}Kr are based primarily on the mean field deduced[8] for n-^{89}Y. The available data for scattering of neutrons from ^{89}Y do not span as large an energy range as was the case for n-^{40}Ca and n-^{208}Pb, but they do include extensive measure-

ments[10] for $1.5 < E < 10$ MeV. Also there are measurements[11,12] of neutron scattering from ^{89}Y at 8, 10, 12, 14, and 17 MeV and of analyzing powers of 10, 14, and 17 MeV. The iterative-moment analysis[8] was extended to 40 MeV using a global model[11] that was based partly on the n-^{89}Y distributions at 10, 14, and 17 MeV.

Other neutron scattering data related to the mean field are the neutron total cross sections in the resonance region. We use the term "resonance region" to designate the positive neutron energy domain of a few hundred keV where the level density is small enough to allow measurement and analysis of the resonances by a high-resolution experiment followed by a multilevel R-matrix analysis. A unique feature of such an analysis is that it yields scattering functions for individual partial waves. If an adequate number of levels is observed, these functions can be averaged over energy[13–15] for comparison to the mean-field predictions for the individual partial waves. In the spirit of the dispersive model, we expect that an extrapolation downward from energies of several MeV will be as successful for the resonance region as it is for the more distant extrapolation to the bound states.

Here, we emphasize the resonance region; we examine the predictions of the dispersive optical model for that region in more detail than in previous works. In the dispersive OMP analysis[6] of n-^{208}Pb, predictions from extrapolation into the resonance region were compared to the results of an R-matrix analysis;[16,17] however, the comparison was given little emphasis because the region included only a few resonances. For the recent analysis[9] of the n-^{90}Zr mean field, the empirical s- and p-wave strength functions and the potential scattering radius R' were included as constraints; however, those empirical functions contain less information than do the more detailed scattering functions considered here.

Our data for the resonance region come from recent measurements[18] of the neutron total cross section for ^{86}Kr. The measurements were made with good energy resolution from 0.015 to 25 MeV, and a detailed R-matrix analysis was made for the resolved resonance region below 0.96 MeV. That analysis provides us with accurate scattering functions for the $s_{1/2}$, $p_{1/2}$, and $p_{3/2}$ partial waves and good estimates of the functions for d waves. Here, we average those scattering functions over energy for the individual partial waves and compare them to the functions predicted by extrapolation of the model from higher energies. The parametrization at higher energies requires empirical differential cross sections. Since there are no such data for ^{86}Kr, our procedure is to extrapolate on the basis of the mean field obtained from the iterative-moment analysis[8] of scattering data for n-^{89}Y. Since ^{89}Y and ^{86}Kr are similar nuclei, each having a filled 50-neutron shell, only minor changes are required for going from one nucleus to the other. We also extrapolate further into the bound state region, much as in the previous studies for n-^{40}Ca and n-^{208}Pb.

Our presentation is as follows. In Sec. II we review and formulate the dispersive OMP with the DR constraint. In Sec. III we review the parametrization of the model[8] for n-^{89}Y, make assumptions for the shape of the form factors, and make small adjustments for conversion to n-^{86}Kr. In Sec. IV we check on the validity of this mean field in the MeV region by showing that it gives a good description of the observed[18] neutron total cross section for ^{86}Kr for the energy region from 2 to 25 MeV. In Sec. V we compare the predicted energies of the bound states with the empirical level structure. In Sec. VI we deduce average scattering functions from the R-matrix parameters for the resonance region and compare these with the predictions from the model. Section VII is a summary discussion of the three energy regions of the preceding sections, and Sec. VIII is our conclusion.

II. FORMULATION OF THE MODEL

We begin by introducing a translation of the energy variable. Nearly all neutron OMP analyses of the past, not only for individual nuclei but also for "global" models of many nuclei, have been formulated in terms of the energy E of the incident neutron. In other words the zero of the energy scale corresponds to the neutron separation energy for the compound nucleus. Since the mean field $\mathcal{M}(r;E)$ is continuous in energy with no special behavior at the neutron separation energy, it is reasonable that a different reference energy may be more useful. Indeed, an empirical study[19] of the influence of the symmetry potential on various nuclei has shown that a more consistent symmetry potential is obtained if the energy is measured relative to the Fermi energy E_F. Also the significant energy for the DR is relative to E_F. Therefore, we introduce the shifted energy variable $\mathcal{E}$;

$$\mathcal{E}=E-E_F \ . \tag{2.1}$$

Except for this translation in energy, our notation follows Refs. 6 and 7 as much as possible. We redefine the mean central field in terms of the new energy variable;

$$\mathcal{M}(r;\mathcal{E})=\mathcal{V}(r;\mathcal{E})+i\mathcal{W}(r;\mathcal{E}) \ . \tag{2.2}$$

The real part can be written in the form

$$\mathcal{V}(r;\mathcal{E})=\mathcal{V}_H(r;\mathcal{E})+\Delta\mathcal{V}(r;\mathcal{E}) \ , \tag{2.3}$$

where $\mathcal{V}_H(r;\mathcal{E})$ is the local equivalent to the Hartree-Fock potential and $\Delta\mathcal{V}(r;\mathcal{E})$ is the dispersive contribution, which is connected to the imaginary potential by the dispersion relation, DR,

$$\Delta\mathcal{V}(r;\mathcal{E})=\frac{\mathrm{P}}{\pi}\int_{-\infty}^{\infty}\frac{\mathcal{W}(r;\mathcal{E}')d\mathcal{E}'}{\mathcal{E}'-\mathcal{E}} \ , \tag{2.4}$$

where P denotes the principal value integral. The energy dependence of the Hartree-Fock-type field $\mathcal{V}_H(r;\mathcal{E})$ is expected to be quite smooth. In contrast, the dispersive correction $\Delta\mathcal{V}(r;\mathcal{E})$ has a strong energy dependence, particularly near $\mathcal{E}=0$.

To apply the DR we need $\mathcal{W}(r;\mathcal{E})$ at both positive and negative energies. As in Refs. 2–7 we assume symmetry with respect to the Fermi energy;

$$\mathcal{W}(r;\mathcal{E})=\mathcal{W}(r;-\mathcal{E}) \ . \tag{2.5}$$

The resulting real dispersive correction is skew symmetric about $\mathcal{E}=0$. Thus, at the Fermi energy the full central real mean field becomes identical to the Hartree-

Fock contribution, which we parametrize with a Woods-Saxon form with shape parameters that are independent of energy;

$$\mathcal{V}_H(r;\mathcal{E})=V_H(\mathcal{E})f(X_H)\ , \tag{2.6}$$

$$f(X_H)=[1+\exp(X_H)]^{-1}\ , \tag{2.7}$$

$$X_H=(r-R_H)/\partial_H\ , \tag{2.8}$$

$$R_H=r_H A^{1/3}\ . \tag{2.9}$$

For the imaginary field we make the usual division into surface and volume components;

$$\mathcal{W}(r;\mathcal{E})=\mathcal{W}_s(r;\mathcal{E})+\mathcal{W}_v(r;\mathcal{E})\ , \tag{2.10}$$

and assume, as for the ^{40}Ca and ^{208}Pb dispersive OMP analyses,[6,7] that the volume part has the same energy-independent shape as for the Hartree-Fock field,

$$\mathcal{W}_v(r;\mathcal{E})=W_v(\mathcal{E})f(X_H)\ . \tag{2.11}$$

With this assumption the integration of the dispersive volume correction involves only the well depths,

$$\Delta V_v(\mathcal{E})=\frac{\mathrm{P}}{\pi}\int_{-\infty}^{\infty}\frac{W_v(\mathcal{E}')d\mathcal{E}'}{\mathcal{E}'-\mathcal{E}}\ . \tag{2.12}$$

Furthermore, the total real volume potential $V_v(r;\mathcal{E})$ involves a simple sum of well depths,

$$\mathcal{V}_v(r;\mathcal{E})=V_v(\mathcal{E})f(X_H)\ , \tag{2.13}$$

$$V_v(\mathcal{E})=V_H(\mathcal{E})+\Delta V_v(\mathcal{E})\ . \tag{2.14}$$

For the surface component we make the usual assumption that the form factor is the radial derivative of a Woods-Saxon factor and also assume, as for the ^{40}Ca and ^{208}Pb analyses of Refs. 6 and 7, that the geometry is independent of energy;

$$\mathcal{W}_s(r;\mathcal{E})=-4a_s W_s(\mathcal{E})\frac{d}{dr}f(X_s)\ , \tag{2.15}$$

with the parameters r_s and a_s. Then the surface dispersive term has the same form factor;

$$\Delta\mathcal{V}_s(r;\mathcal{E})=-4a_s\Delta V_s(\mathcal{E})\frac{d}{dr}f(X_s)\ , \tag{2.16}$$

$$\Delta V_s(\mathcal{E})=\frac{\mathrm{P}}{\pi}\int_{-\infty}^{\infty}\frac{W_s(\mathcal{E}')d\mathcal{E}'}{\mathcal{E}'-\mathcal{E}}\ . \tag{2.17}$$

In the following section we first parametrize the model for n-^{89}Y and then convert to n-^{86}Kr. For this purpose we assume that each of the potential strengths for the mean field could have a symmetry component proportional to the nuclear asymmetry coefficient, $\eta=(N-Z)/A$;

$$V_H(\mathcal{E})=V_H^0(\mathcal{E})+\eta V_{H1}(\mathcal{E})\ , \tag{2.18}$$

$$W_v(\mathcal{E})=W_v^0(\mathcal{E})+\eta W_{v1}(\mathcal{E})\ , \tag{2.19}$$

$$W_s(\mathcal{E})=W_s^0(\mathcal{E})+\eta W_{s1}(\mathcal{E})\ , \tag{2.20}$$

where the leading terms on the right-hand sides are independent of the asymmetry coefficient.

In addition to its central component, Eq. (2.1), the mean field contains a spin-orbit component for which we take the standard real form,

$$\mathcal{V}_{\mathrm{SO}}(r)=\boldsymbol{\sigma}\cdot\boldsymbol{l}\left[\frac{\hbar}{m_\pi c}\right]^2 V_{\mathrm{SO}}\frac{1}{r}\frac{d}{dr}f(X_{\mathrm{SO}})\ , \tag{2.21}$$

with energy-independent parameters V_{SO}, r_{SO}, and a_{SO}. Since $\mathcal{V}_{\mathrm{SO}}(r)$ is assumed to be real, there is no dispersive contribution.

This is a "fixed-geometry" model.[6,7] Actually, there have been OMP analyses indicating that the surface shape parameters depend on energy, with r_s increasing and a_s decreasing for decreasing neutron energies below 10 MeV. Such a dependence was found for ^{89}Y from the measurements[10] which were the basis for the low-energy part of the model to be used here. Similar energy dependences were found for neutron scattering[20,6] from ^{208}Pb and scattering[21] from ^{93}Nb. Nevertheless, we make the approximation of fixed geometry for the following reasons. The introduction of an energy-dependent shape into the DR requires that $\Delta\mathcal{V}(r;\mathcal{E})$ be calculated by numerical integration, and it leads to surface dispersive shapes that deviate strongly from Woods-Saxon derivatives. A recent study[22] of these unusual shapes for the case of n-^{208}Pb showed that they have strong influence on the predicted cross sections. The study indicated that a more consistent description of the data is achieved by replacing the energy dependence in the radius by a dependence on angular momentum. Similar conclusions were reached from a more limited study[23] of ^{89}Y. Therefore the earlier empirical evidences for energy dependence should be reexamined with inclusion of the DR. A proper treatment of the possible energy and angular momentum dependence for the present case should include detailed reanalysis of the observed[10] scattering distributions for neutrons from ^{89}Y. For simplicity, we use the fixed-geometry model; its use for a broad range of positive and negative energies is found to be very fruitful, much as it was in Refs. 6 and 7 for n-^{40}Ca and n-^{208}Pb.

III. PARAMETRIZATION OF THE MEAN FIELD

A. Model for n-^{89}Y

In the iterative-moment analysis[8] of n-^{89}Y, the diffuseness of the Hartree-Fock potential was assumed to be constant and the resulting Hartree-Fock radius was found to be essentially constant. We adopt those values;

$$r_H=1.24\text{ fm},\quad a_H=0.7\text{ fm}\ . \tag{3.1}$$

These are nearly the same as the values, 1.24 and 0.68 fm, found for n-^{208}Pb from the dispersive OMP analysis.[6]

The n-^{208}Pb analysis covered a broad energy range and showed that the well depth for the local equivalent of the Hartree-Fock potential decreases exponentially with energy. The smaller range of energies considered here allows us to use a linear approximation;

$$V_H(\mathcal{E})=V_H(0)+\alpha\mathcal{E}\ . \tag{3.2}$$

For n-^{89}Y with the parameters of Eq. (3.1), the iterative-

moment analysis[8] gave

$$V_H(\mathcal{E}) = -4.75 + 0.29\mathcal{E} \text{ MeV} . \quad (3.3)$$

For the imaginary component the analysis[8] provides us with the volume integral per nucleon, $J_{\mathcal{W}}(\mathcal{E})$, for the full imaginary potential. The parameters of $J_{\mathcal{W}}(\mathcal{E})$ were deduced[8] from a least-squares fit to a combination of two sets of data for $12 < \mathcal{E} < 49$ MeV. For the lower part of this energy range, $12 < \mathcal{E} < 19$ MeV, the data used were ten empirical volume integrals which Lawson *et al.*[10] obtained by conventional OMP analyses of the scattering of 2.8- to 10-MeV neutrons on ^{89}Y. For those energies the volume term $W_v(r;\mathcal{E})$ is negligible. For the higher energies, $19 < \mathcal{E} < 49$ MeV, the basis was a global parametrization by Walter and Guss[11] that included both volume and surface terms. Mahaux and Sartor[8] parametrized $J_W(\mathcal{E})$ using the form suggested by Brown and Rho;[24]

$$J_{\mathcal{W}}(\mathcal{E}) = B\frac{\mathcal{E}^2}{(\mathcal{E}^2+\mathcal{E}_1^2)} , \quad (3.4a)$$

$$B = -94 \text{ MeV fm}^3 , \quad (3.4b)$$

$$\mathcal{E}_1 = 9.8 \text{ MeV} . \quad (3.4c)$$

We note that B is the asymptotic value of $J_W(\mathcal{E})$ for large $|\mathcal{E}|$ and $\mathcal{E}_1$ is the $|\mathcal{E}|$ for which $J_{\mathcal{W}}(\mathcal{E}) = B/2$. The full dispersive contribution to the real potential can be evaluated analytically;[24]

$$J_{\Delta\mathcal{V}}(\mathcal{E}) = \frac{\mathrm{P}}{\pi}\int_{-\infty}^{\infty}\frac{J_{\mathcal{W}}\mathcal{E}'d\mathcal{E}'}{\mathcal{E}'-\mathcal{E}} \quad (3.5a)$$

$$= B\frac{\mathcal{E}_1\mathcal{E}}{(\mathcal{E}^2+\mathcal{E}_1^2)} . \quad (3.5b)$$

The solid curves in Figs. 1(a) and 1(b) represent, respectively, $J_{\mathcal{W}}(\mathcal{E})$ and $J_{\Delta\mathcal{V}}(\mathcal{E})$.

The full imaginary potential is a sum of surface and volume components. Empirical evidence shows that the volume component $J_{\mathcal{W}_v}(\mathcal{E})$ rises approximately linearly with energy from a threshold at about $\mathcal{E} = 15$ MeV. For example, the ^{208}Pb$+n$ threshold[6] is 16 MeV, and the global model of Ref. 11 has a threshold corresponding to $\mathcal{E} = 15.4$ MeV for ^{89}Y and 14 MeV for ^{86}Kr. We assume a 15-MeV threshold. The empirical evidence also indicates that the surface contribution decreases with energy such that the volume component becomes dominant at approximately $\mathcal{E} = 60$ MeV. To satisfy these requirements as well as the symmetry assumption, Eq. (2.5), we introduce the parametrization;

$$J_{\mathcal{W}_v}(\mathcal{E}) = 0.0, \quad |\mathcal{E}| < 15 \text{ MeV} , \quad (3.6a)$$

$$J_{\mathcal{W}_v}(\mathcal{E}) = 30 - 2|\mathcal{E}| \text{ (MeV fm}^3\text{)}, \quad 15 < |\mathcal{E}| < 62 \text{ MeV} , \quad (3.6b)$$

$$J_{\mathcal{W}_v}(\mathcal{E}) = B, \quad |\mathcal{E}| > 62 \text{ MeV} . \quad (3.6c)$$

These linear segments are represented with short dashes in Fig. 1(a). [The differences between $J_{\mathcal{W}_v}(\mathcal{E})$ and $J_{\mathcal{W}}(\mathcal{E})$ are to be neglected for $\mathcal{E} > 62$ MeV]. Analytical evaluation of the DR of these linear segments yields the volume dispersive contribution $J_{\Delta\mathcal{V}_v}(\mathcal{E})$, which is represented by the short-dashed curve in Fig. 1(b).

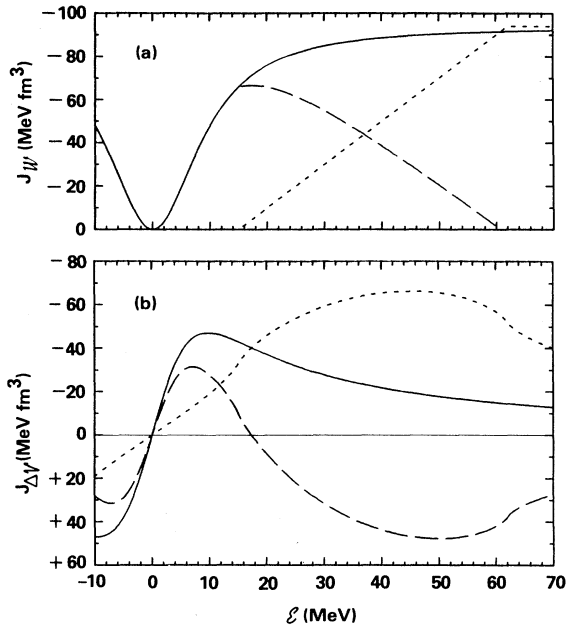

FIG. 1. (a) Imaginary and (b) dispersive volume integrals per nucleon versus the energy $\mathcal{E}$ relative to the Fermi energy for the neutron-^{89}Y mean field. Short-dashed curves represent surface terms, long-dashed curves represent volume terms and the solid curves are the sums of the surface and volume terms. In (a) the difference between the solid and short-dashed curves for $\mathcal{E} > 61$ MeV is negligible.

The surface imaginary volume integral $J_{\mathcal{W}_s}(\mathcal{E})$ is found by subtracting the volume component from the total,

$$J_{\mathcal{W}_s}(\mathcal{E}) = J_{\mathcal{W}}(\mathcal{E}) - J_{\mathcal{W}_v}(\mathcal{E}) , \quad (3.7)$$

with the restriction that $\mathcal{J}_{\mathcal{W}_s}(\mathcal{E}) = 0$ for energies above the cutoff energy near 61 MeV. The result is represented by the long-dashed curve in Fig. 1(a). The surface dispersive term $J_{\Delta\mathcal{V}_s}(\mathcal{E})$ is also found by subtraction,

$$J_{\Delta\mathcal{V}_s}(\mathcal{E}) = J_{\Delta\mathcal{V}}(\mathcal{E}) - J_{\Delta\mathcal{V}_v}(\mathcal{E}) , \quad (3.8)$$

and is represented by the long-dashed curve in Fig. 1(b).

The final step in parametrization of the potential for ^{89}Y is the assumption of specific form factors. Regarding the volume component, we have already assumed in Sec. II that the shape parameters are the same as for the Hartree-Fock potential, Eq. (3.1). This means that the volume and dispersive depths, $W_v(\mathcal{E})$ and $\Delta V_v(\mathcal{E})$, are given by the ratios $J_{\mathcal{W}_v}(\mathcal{E})/G$ and $J_{\Delta\mathcal{V}_v}(\mathcal{E})/G$, where $G = 9.25$ fm^3 for the parameters, $r_w = 1.24$ fm and $a_w = 0.7$ fm. The volume imaginary component is of little interest in itself for the present work because its threshold, $|\mathcal{E}| = 15$ MeV, is outside most of the energies considered here. However, its dispersive contribution makes a significant correction to the Hartree-Fock depth for energies below the threshold. From Fig. 1(b) we see that ΔV_v is nearly linear in energy for $|\mathcal{E}| < 15$ MeV. Thus, from

Eqs. (2.14) and (3.3) we find approximately,

$$V_v(\mathcal{E}) = -47.5 + 0.08\mathcal{E} \text{ MeV}, \quad |\mathcal{E}| < 15 \text{ MeV} . \tag{3.9}$$

For the surface imaginary component, we assumed in Sec. II that the shape parameters are to be independent of energy. We take the same parameters as used for the analysis[6] of n-^{208}Pb;

$$r_s = 1.27 \text{ fm and } a_s = 0.58 \text{ fm} . \tag{3.10}$$

These are typical empirical values[11,25] for neutrons in the energy range 10–40 MeV.

For the spin-orbit component, Eq. (2.18), we adopt the same parameters as for the ^{208}Pb analysis of Ref. 6;

$$V_{SO} = 5.75 \text{ MeV}, \quad r_{SO} = 1.10 \text{ fm}, \quad a_{SO} = 0.50 \text{ fm} . \tag{3.11}$$

These are also typical empirical values. This spin-orbit potential, in terms of its volume integral, is intermediate between that deduced in Ref. 10 from scattering of 8- and 10-MeV neutrons from ^{89}Y and that deduced in Ref. 12 from measurements of analyzing power for 10-, 14-, and 17-MeV neutron scattering from ^{89}Y.

B. Transformation to n-^{86}Kr

There are three nuclear properties which make our mean field different for ^{86}Kr than for ^{89}Y: these are (i) the radius is smaller for ^{86}Kr than for ^{89}Y, (ii) the Fermi energy E_F is less negative for ^{86}Kr than for ^{89}Y, and (iii) ^{86}Kr has three favor protons than ^{89}Y

The smaller radius for ^{86}Kr is introduced via the conventional $A^{1/3}$ dependences in the various form factors for the model

We have included effects of the difference in E_F in our formulation by expressing the field as a function of the energy $\mathcal{E}$ relative to E_F. For n-^{86}Kr we take E_F to be midway between the 5.515-MeV binding energy for the $d_{5/2}$ ground state in ^{87}Kr and the 9.863-MeV neutron separation energy for ^{86}Kr, which leaves ^{85}Kr in its $g_{9/2}$ ground state. Thus

$$E_F = -7.7 \text{ MeV} . \tag{3.12}$$

This is to be compared to the value -9.1 MeV, assumed for the n-^{89}Y analyses.[8,10] For a given neutron energy E, this 1.4-MeV difference in E_F affects the components of the potential that are energy dependent. For the imaginary component the effect is significant at low energies; for a neutron energy of 0.5 MeV, which is the center of the resonance region to be analyzed in Sec. VI, the surface imaginary depth for ^{86}Kr is predicted to be 16% less than that for ^{89}Y at the same neutron energy. The effect is less for the central real depth $V_v(\mathcal{E})$ because the energy coefficient in Eq. (3.9) is small; thus, at a given neutron energy, the difference in E_F makes $V_V(\mathcal{E})$ only 0.1 MeV deeper for ^{86}Kr than for ^{89}Y.

Changes in the potential associated with the fewer protons in ^{86}Kr result from the symmetry potentials, Eqs. (2.18)–(2.20), because the asymmetry coefficient is slightly larger for ^{86}Kr than for ^{89}Y;

$$\Delta\eta = {}^{86}\eta - {}^{89}\eta = 0.039 . \tag{3.13}$$

For the Hatree-Fock field we assume $V_{H1} = 15$ MeV. From Eqs. (2.18), (3.3), and (3.12) we then find for the n-^{86}Kr system,

$$V_H^{86}(\mathcal{E}) = V_H^{89}(\mathcal{E}) + \Delta\eta V_{H1} , \tag{3.14a}$$

$$V_H^{86}(\mathcal{E}) = -46.9 + 0.29\mathcal{E} \text{ MeV} . \tag{3.14b}$$

We have neglected the energy dependence in the symmetry potential[25] because its effect on the change in the energy coefficient for $V_H(\mathcal{E})$ is negligible. Our choice of $V_{H1} = 15$ MeV is consistent with Rapaport's review.[25] The following comparison shows that it is also consistent with the difference between empirical[6,8] Hartree-Fock potentials for n-^{89}Y and n-^{208}Pb. The model deduced[8] for n-^{208}Pb by the dispersive OMP analysis has the same Hartree-Fock radius as for n-^{89}Y but a smaller depth, $V_H(0) = -46.4$ MeV. If we adjust V_{H1} to reproduce the difference in $V_H(0)$ between n-^{89}Y and n-^{208}Pb, we find $V_{H1} = 12.5$ MeV, in good agreement with our assumed value. A similar comparison between the model for n-^{89}Y and that deduced[6] from the dispersive OMP analysis for n-^{40}Ca yields a much larger value, $V_{H1} = 90$ MeV. However, the latter comparison is complicated by the fact that the radius r_H for the n-^{40}Ca model is only 1.18 fm. Therefore, as discussed in Ref. 6, the central density is higher for ^{40}Ca and the deeper well for ^{40}Ca may result partially from this larger density.

The following asymmetry correction for the imaginary potential is comparable to the uncertainty in the potential itself; nevertheless, we believe it is worth making because it is in the right direction and about the right magnitude. Rapaport[25] concluded that the volume integral of the full imaginary symmetry potential is about 50% larger than the main isoscalar component for 10-MeV neutrons, and that it decreases to zero at about $E = 80$ MeV. The global model of Walter and Guss[11] has only a surface symmetry term. To describe these empirical properties approximately, we assume

$$W_{s1}(\mathcal{E}) = -1.5 W_s^0(\mathcal{E}) , \tag{3.15}$$

$$W_{v1}(\mathcal{E}) = 0.0 , \tag{3.16}$$

where Eq. (3.15) includes an implicit assumption that the empirical symmetry potential can be extrapolated to neutron energies below 10 MeV. From Eqs. (2.20), (3.13), and (3.15), we find

$$W_s^{86}(\mathcal{E}) = 0.94 W_s^{89}(\mathcal{E}) . \tag{3.17}$$

It follows from the DR that the surface dispersive term is reduced by the same factor;

$$\Delta V_s^{86}(\mathcal{E}) = 0.94 \Delta V_s^{89}(\mathcal{E}) . \tag{3.18}$$

We note that, at the center of the resonance region, the combined effects of the smaller $|E_F|$ and the fewer protons in ^{86}Kr reduce the imaginary potential depth by 21% relative to that for ^{89}Y, for the same neutron energy. Furthermore, the depth for ^{86}Kr is only 39% of the

asymptotic value. That is significant for the predictions of neutron strength functions to be discussed in Sec. VI.

IV. NEUTRON AVERAGED TOTAL CROSS SECTIONS FOR ^{86}Kr

In Fig. 2 the smooth curve represents the total cross section predicted for ^{86}Kr from our model for neutron energies from 0.01 to 25 MeV, and the histograms represent cross sections deduced by averaging over energy of the high-resolution cross sections reported in Ref. 18. The width of each histogram is the averaging interval and the height of the vertical symbol on each histogram represents the uncertainty from counting statistics. At low energies the histograms have large vertical fluctuations because the resonance fluctuations have not been completely removed by averaging.

The predicted curve is seen to be in overall good agreement with the observations. For $2 < E < 25$ MeV the prediction is very good, and for $E < 0.5$ MeV it represents a good average to the data. However, for the intermediate region, $0.5 < E < 2$ MeV, and particularly for $0.5 < E < 1$ MeV, the predicted curve falls generally below the histograms. In Sec. VI we examine the individual partial waves that contribute in the latter region.

V. EXTRAPOLATION TO NEGATIVE ENERGIES

The left-hand diagram in Fig. 3 represents the energies for particle and hole states predicted from only the Hartree-Fock component of the field, and the center diagram represents the level structure predicted from the full real part of the model. We compare these two structures further in the discussion of Sec. VII.

The observed structure is shown at the right in Fig. 3. For $E > E_F$ the observed levels are taken from the "adopted" ^{87}Kr levels in the Nuclear Data Sheets[26] with the restriction that only those with significant spectroscopic factors for ^{86}Kr(d,p) stripping[27,28] are retained here. The spectroscopic factors are shown at the far right for individual levels or groups of levels. For the hole states, $E < E_F$, the levels plotted are based on those observed[29,30] by the ^{86}Kr(d,t) and ^{86}Kr$(^3$He$,\alpha)$ pickup reactions, except that we include J^π values only for the three states which were assigned in the "adopted" level scheme from the Nuclear Data Sheets[31] for ^{85}Kr. The $\frac{9}{2}^+$ level, which is the ground state of ^{85}Kr, is plotted at the neutron separation energy of -9.863 MeV. The spectroscopic factors for the highest three hole states are from the $(^3$He$,\alpha)$ pickup measurement[30] with the same unit normalization for the $\frac{1}{2}^-$ hole state. In Sec. VII we compare the observed and predicted structures.

VI. PARTIAL-WAVE PREDICTIONS FOR 0–1-MeV NEUTRONS

The histograms in Fig. 2 were obtained by averaging of cross sections that were orginally measured[18] with good

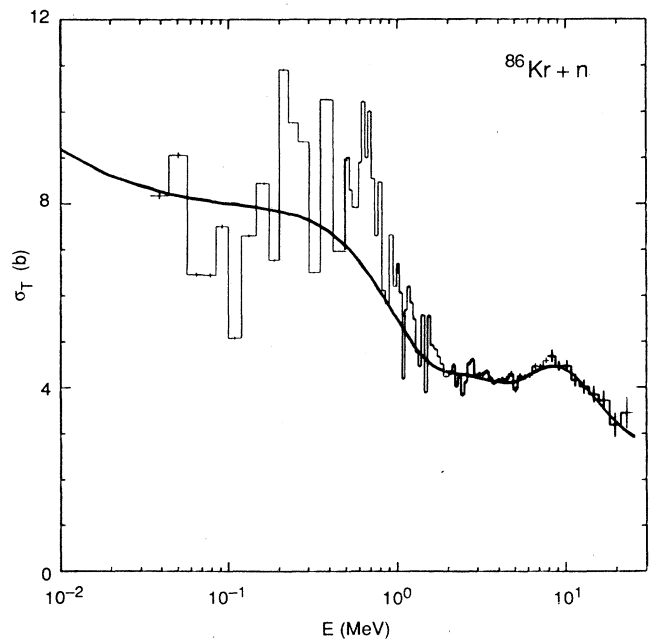

FIG. 2. Total cross section of ^{86}Kr vs neutron energy. The solid curve is predicted from the model. The histograms represent averages over energy of cross sections that were orginally measured with high resolution in Ref. 18. The vertical symbol on each histogram represents the uncertainty from counting statistics.

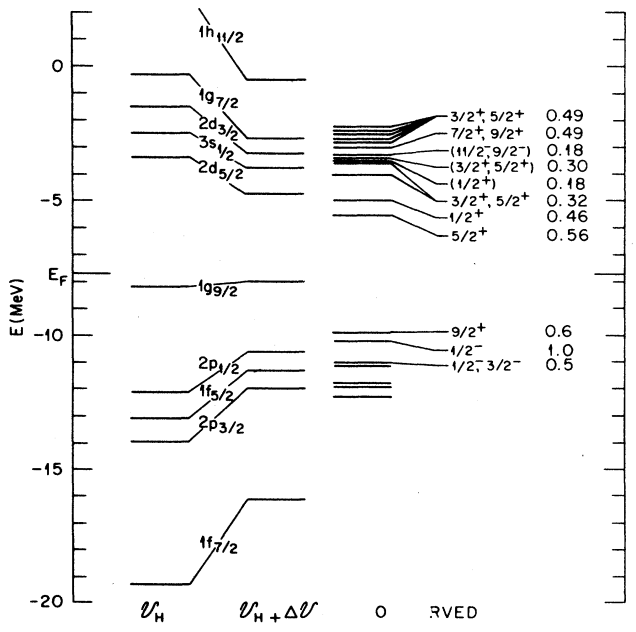

FIG. 3. Energies of the valence neutron single-particle states in ^{86}Kr. The diagrams labeled V_H and $V_H + \Delta V$ were calculated, respectively, from the Hartree-Fock potential and from the real part of the full potential. The diagram labeled "observed" shows the experimental energy levels, their J^π assignments, and the empirical spectroscopic factors. An assignment of two J^π values to a single level means that one or the other is correct; values in parentheses are favored assignments.

energy resolution to reveal the resonance structure. In Ref. 18 the original unaveraged resonance structure was fit in detail using the R-matrix formalism for the neutron energies from $E_l=0.015$ MeV to $E_u=0.96$ MeV. Since only the neutron entrance channel is important in this case, the R matrix reduces to a single-channel R function such that the scattering function $S_{lj}(E)$ for orbital angular moment l and total angular momentum $j=l\pm\frac{1}{2}$ can be written

$$S_{lj}(E)=e^{-2i\varphi l(E)}\frac{1+iP_l(E)R_{lj}(E)}{1-iP_l(E)R_{lj}(E)} , \tag{6.1}$$

where $P_l(E)$ and $\varphi_l(E)$ are the penetrability and the hard-sphere phase shift evaluated at the channel radius. A channel radius must be chosen but its value is not critical; for the present analysis it was 6.4 fm. In Eq. (6.1) the boundary condition has been set equal to the shift factor at all energies. The R function $R_{lj}(E)$ is a sum over the n resonances with quantum numbers l and j that are observed within the experimental domain, plus an external R function which accounts for the influence of levels outside of the domain;

$$R_l(E)=\sum_{\lambda=1}^{n}\frac{\gamma_{lj\lambda}^2}{E_{lj\lambda}-E}+R_{lj}^{\text{ext}}(E) , \tag{6.2}$$

where $E_{lj\lambda}$ and $\gamma_{lj\lambda}^2$ are the energy and reduced width of the λ th level.

The fitted R-matrix parameters were presented in Ref. 18 in tables and figures. Here we reproduce the essential parts of the figures. In Fig. 4 the solid curves represent $R_{lj}^{\text{ext}}(E)$. The vertical symbols show uncertainties estimated at energies where the resonance-potential interference patterns provide the best information. These uncertainties increase with l because of the decreasing penetrability $P_l(E)$ of the centrifugal barrier. It is this decrease in penetrability thta limits our study to s-, p-, and d-wave neutrons.

The "staircases" in Fig. 5 represent the cumulative sums of reduced widths up to the neutron energy E. Each riser represents a reduced width, $\gamma_{lj\lambda}^2$, and each tread is the spacing between adjacent levels. The different scales of the ordinates should be noted; the sums of p-wave reduced widths are about ten times those for s or d waves. The error bars at the tops of the staircases are not experimental uncertainties; they are deduced from the fractional uncertainty, $(2/n)^{1/2}$, that would occur in the full sum if the observed n widths were drawn at random from a Porter-Thomas distribution.

We emphasize that the s- and p-wave parametrizations represented in Figs. 4 and 5, along with the R-matrix boundary conditions, provide complete descriptions of the s- and p-wave scattering functions in the experimental domain $[E_l,E_u]$. This statement is qualified only by the presence of small experimental uncertainties. For these partial waves, therefore, there would be little to gain from a further measurement such as a measurement of differential cross sections. The information for d waves is less detailed because of the centrifugal barrier. In particular, as discussed in Ref. 18, there are experimental uncertainties in the separation of the d-wave widths into the $d_{3/2}$ and $d_{5/2}$ components.

For comparison to the scattering function $S_{lj}^{\text{OM}}(E)$ predicted from the model, we must average the empirical function over energy. That can be performed numerically; calculations[14] with various averaging functions have shown that the results are insensitive to the shape of the averaging function. The average, $\langle S_{lj}(E)\rangle$, can be presented in various ways. For example, it could be presented in terms of complex phase shifts or in terms of compound and shape-elastic cross sections. Our choice is to expand the average in terms of a complex R function, *using the same boundary conditions as for the R-matrix analysis of the data;*

$$\langle S_{lj}(E)\rangle=e^{-2i\varphi_l(E)}\frac{1+iP_l(E)\mathcal{R}_{lj}(E)}{1-iP_l(E)\mathcal{R}_{lj}(E)} , \tag{6.3}$$

$$\mathcal{R}_{lj}(E)=\tilde{R}_{lj}(E)+i\pi\tilde{s}_{lj}(E) . \tag{6.4}$$

This complex R function varies slowly with energy.

The studies[14,15] with numerical averaging showed that $\mathcal{R}_{lj}(E)$ can be obtained approximately by direct comparisons to the R-matrix parameters plotted in Figs. 4 and 5. This equivalence also has an analytic basis.[13–15] Therefore the difficult numerical integrations are not necessary. Approximately,

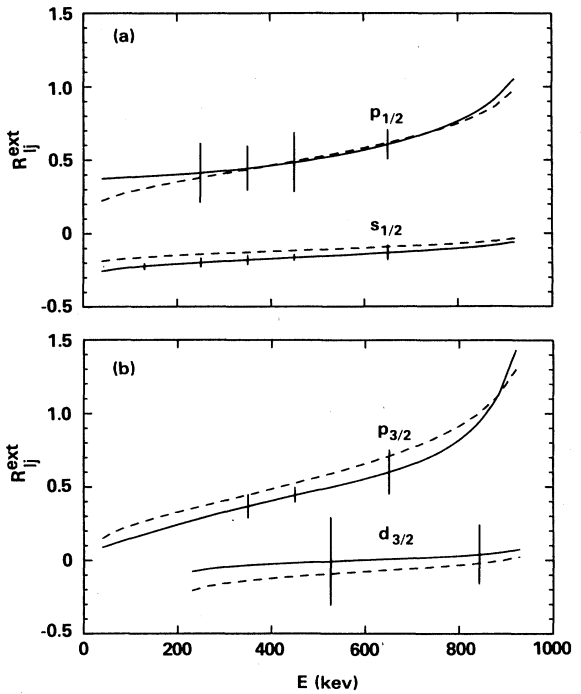

FIG. 4. External R functions for 0.015-MeV to 0.96-MeV neutron scattering from ^{86}Kr. The solid curves were determined in Ref. 17 from an R-matrix analysis of resonances observed in the neutron total cross section. Vertical symbols represent uncertainties at selected energies. Dashed curves are deduced from R-function expansions of the model scattering functions. The assumed R-matrix channel radius is 6.4 fm for all curves.

$$\sum_{\lambda=1}^{\lambda=k} \gamma_{lj\lambda}^2 = \int_{E_l}^{E_k} \tilde{s}_{lj}(E')dE' , \tag{6.5}$$

$$R_{lj}^{\text{ext}}(E) = \tilde{R}_{lj}(E) - \mathrm{P}\int_{E_l}^{E_u} \frac{\tilde{s}_{lj}(E')dE'}{E'-E} , \tag{6.6}$$

where P denotes the principal value integral. The left-hand sides of these equations are the empirical parametrizations presented in Figs. 4 and 5. If simple functional forms for $\tilde{R}_{lj}(E)$ and the "strength function" $\tilde{s}_{lj}(E)$ are assumed and then parametrized to achieve consistency of the right-hand sides with the empirical left-hand sides of these two equations, those parametrized functions can be inserted into Eqs. (6.3) and (6.4) to calculate approximate average scattering functions. In Ref. 18 the functions $\tilde{R}_{lj}(E)$ and $\tilde{s}_{lj}(E)$ were so parametrized.

Here, we reverse that procedure in order to compare the predicted scattering functions, $S_{lj}^{OM}(E)$, to the averaged empirical functions. We expand $S_{lj}^{\text{OM}}(E)$ in the same manner as in Eq. (6.3) *with the same boundary conditions,*

$$S_{lj}^{\text{OM}}(E) = e^{-2i\varphi_l(E)} \frac{1+iP_l(E)\mathcal{R}_{lj}^{\text{OM}}(E)}{1-iP_l(E)\mathcal{R}_{lj}^{\text{OM}}(E)} , \tag{6.7}$$

$$\mathcal{R}_{lj}^{\text{OM}}(E) = \tilde{R}_{lj}^{\text{OM}}(E) + i\tilde{s}_{lj}^{\text{OM}}(E) . \tag{6.8}$$

The curves in Fig. 6 represent the resulting model strength functions, $\tilde{s}_{lj}^{\text{OM}}(E)$. We then introduce the model functions $\tilde{R}_{lj}^{\text{OM}}(E)$ and $\tilde{s}_{lj}^{\text{OM}}(E)$ into the right-hand sides of Eqs. (6.5) and (6.6). In Fig. 4 the dashed curves represent the predicted external R functions; in Fig. 5 the smooth curves represent the predictions for the cumulative strengths.

VII. DISUCSSION

The present study of the n-^{86}Kr interaction in the context of the dispersive optical model potential includes a broad neutron energy region from about -13 to $+25$ MeV, but the unique feature relative to earlier related works is the prediction of the scattering functions for individual partial waves in the region from 0.105- to 0.96-MeV neutrons. It is significant that a model with relatively few parameters succeeds not only in giving a good description of the empirical data over a broad energy region but also in describing finer details in the narrow resonance region.

The basic parametrization came from a model that had been developed by an iterative-moment analysis[8] for the n-^{89}Y mean field. Our use of the model required that we parametrize the form factors; we assumed that all of the shape parameters are independent of energy. This "fixed-geometry" assumption is in keeping with the models[6,7] that were so successful for the n-^{40}Ca and n-^{208}Pb mean fields for broad energy regions. To convert to the n-^{86}Kr interaction, we made small corrections for the real

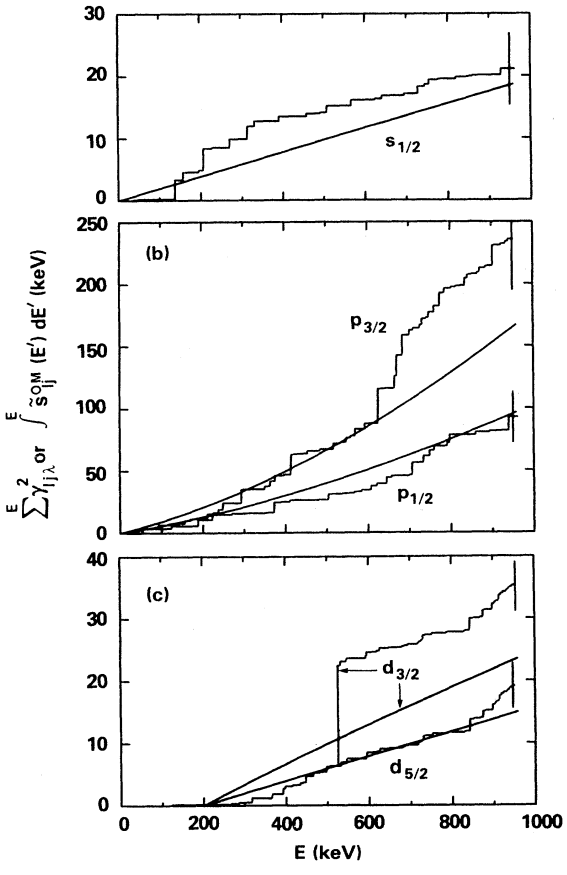

FIG. 5. Cumulated reduced widths and integrals of strength functions for neutron scattering from ^{86}Kr. The staircases represent the summation up to the neutron energy E of the reduced widths determined from the same R-matrix analysis as for Fig. 4. Vertical symbols at the tops of the staircases are uncertainties based on assumed Porter-Thomas distributions of widths. Smooth curves represent integrals up to E of the strength functions predicted from the model. All curves are for an assumed 6.4-fm R-matrix channel radius.

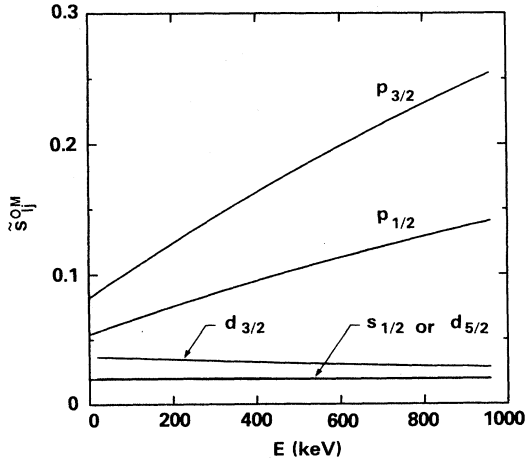

FIG. 6. Neutron strength functions deduced from the predicted scattering functions of the model. The R-function expansion was made using a 6.4-fm channel radius.

and imaginary symmetry potentials. Furthermore, we parametrized the model in terms of the energy relative to the Fermi energy E_F in order to account for the 1.4-MeV difference in E_F between n-^{89}Y and n-^{86}Kr. Full details of the formulation and parametrization were presented in Secs. II and III.

Given the model, we began in Sec. IV and V by comparing its predictions to experimental data for energies both above and below the resonance region. Figure 2 shows that the model provides an excellent description of the energy-averaged total cross section for 2- to 25-MeV neutrons. This success shows that the real and imaginary volume integrals, or similar quantities such as Vr^2 and Wr^2, are well parametrized at higher energies.

In Sec. V we examined the predictions of the model for negative energies. The binding energies for the occupied and unoccupied valence orbits in the real part of the potential are compared in Fig. 3 with the avaliable experimental data. The only empirical parameter introduced into the model from the bound state region was Fermi energy, -7.7 MeV. The observed level structure is shown toward the right-hand side of Fig. 3 and the spectroscopic factors are on the right-hand side. These factors, summed over the observed fragments, give 0.64 for $\frac{1}{2}^+$, 1.67 for the combined $\frac{3}{2}^+$ and $\frac{5}{2}^+$ levels, and 0.49 for the probable $\frac{7}{2}^+$ level. Thus it is reasonable to assume that most of the fragments have been observed. The observed fragmentation makes it difficult to make comparisons to the predicted levels; nevertheless, average comparisons are possible. On average, the predicted energies of the even parity unoccupied states ($3s_{1/2}$, $2d_{3/2}$, $2d_{5/2}$, and $1g_{7/2}$) agree well with the empirical values. The $3s_{1/2}$, $2d_{3/2}$, and $2d_{5/2}$ orbits are of special interest in relation to s-wave and d-wave scattering in the unbound resonance region, as discussed below. For the occupied states the comparison of the predictions to the empirical levels is even less quantitative. We do note that the mean field binds the $1g_{9/2}$ orbit less than observed. Stated in another way, the predicted separation between the $1g_{9/2}$ and $2p_{1/2}$ orbits is 2.6 MeV, whereas the empirical separation is only about 0.5 MeV. Similar empirical separations are found[30] by the pickup reactions on ^{89}Y and ^{90}Zr, which also have closed 50-neutron shells.

To illustrate the special importance of the dispersive terms at negative energies, we plotted at the left in Fig. 3 the level structure predicted from only the Hartree-Fock component of the field. We see that the omission of the dispersive terms spreads out the levels relative to those for the full potential and relative to the observed levels. This shows that the dynamic effects[32] embodied in the DR must be included to describe the observed compressed level structure in the region near the Fermi surface. The excess spreading in the pure Hartree-Fock potential can be attributed to the relatively large and positive energy coefficient, $+0.29$, for $V_H(\mathcal{E})$ in Eq. (3.14b). In contrast, the volume integral of the full potential has a negative coefficient because the coefficients for the added dispersive terms have large negative values in the neighborhood of E_F (see Fig. 1). The fact that the empirical coefficient is negative for the full volume integral has been called the "Fermi surface anomaly." A more familiar or "normal" energy coefficient[11,25] is associated with phenomenological analyses of scattering of 10- to 40-MeV neutrons. For those energies the coefficient for the effective real well depth is about $+0.30$, i.e., about the same positive value as for the Hartree-Fock potential. This is so because the dispersive contribution in that positive energy region has only a weak energy dependence, as shown in Fig. 1(b). (The foregoing discussion of the Fermi surface anomaly could also be made in terms of effectiveness masses.)

Finally, in Sec. VI, we compared the predictions to measurements in the intermediate resonance region, which extends upward to about 1 MeV above the neutron binding energy. The experimental data consist of neutron total cross sections for ^{86}Kr that were measured with high resolution and analyzed[18] by the R-matrix formalism to yield scattering functions for s-, p-, and d-wave neutrons. These functions can be averaged over energy for comparison to those predicted by the mean field for the individual partial waves. We defined the strength functions and external R functions, $\bar{s}_{lj}(E)$ and $R_{lj}^{\rm ext}(E)$, to be used for the comparisons between the predictions and the experiment. In Fig. 4 the empirical and predicted $R_{lj}^{\rm ext}(E)$ are represented by solid and dashed curves, respectively. We see that the predictions are very good, generally within the experimental uncertainties. In Fig. 5 the staircase plots represent the cumulative sums of experimental reduced widths for the partial waves, $s_{1/2}$, $p_{1/2}$, $p_{3/2}$, $d_{3/2}$, and $d_{5/2}$. The smooth curves represent the integrals of the predicted strength functions up to the energy E. Overall these curves agree very well with the staircases. The upper ends of the curves generally agree with the tops of the staircase within the Porter-Thomas uncertainties. We have checked and found that adjustments of the parameters may improve the agreement in Figs. 4 and 5 for some partial waves but, at the same time, worsen it for others so that the overall agreement is no better than already shown.

The general good agreement between the predicted and empirical values in Figs. 4 and 5 is impressive because the model has few adjustable parameters and those were determined almost entirely from measurements of neutron scattering from other nuclei at higher energies. The single parameter chosen specifically for ^{86}Kr was the Fermi energy, $E_F=-7.7$ MeV. That choice and the formulation of the model in terms of the energy relative to E_F are not of trivial consequence because the potentials have strong dependences for energies near E_F and the resonance region is not far removed from E_F. The important energy-dependent quantities can be recognized by reference to Fig. 1, where the center of the resonance region corresponds to $\mathcal{E}=8.2$ MeV. At that energy the depth of the surface imaginary potential has decreased to about half the maximum value which it attains at higher energies, and the surface dispersive depth is at its maximum.

Before proceeding to a more detailed discussion of the resonance region, we discuss our choice of the functions, $\bar{s}_{lj}(E)$ and $R_{lj}^{\rm ext}(E)$, which we used for comparing the experiment to the predictions. Unfortunately, these quantities are not so easily visualized as are the cross sections at higher energies or the binding energies at negative ener-

gies. In fact, $\bar{s}_{lj}$ and R_{lj}^{ext} are not even definite physical quantities because their values depend on the arbitrary R-matrix boundary conditions. For that reason we emphasized in Sec. VI that the predicted and empirical values must be deduced with the same boundary conditions in order to make valid comparisons between theory and experiment. We could have made the comparisons using the compound and shape-elastic cross sections;[33,34] those quantities are invariant relative to the boundary conditions. But we favor the strength functions and external R functions because they allow more direct comparisons and can be interpreted qualitatively to give a good physical picture of the interactions.

To our knowledge this method of comparing the empirical and predicted scattering function was used only once before;[35] that was for an analysis of neutron scattering from ^{32}S. On the other hand, there are many papers in the literature which make comparisons in terms of "conventional" s-wave and p-wave strength functions.[36] It is appropriate, therefore, that we comment on the conventional strength functions in relation to our insistence that the same R-matrix boundary conditions must be used for both the experimental analysis and for the comparison to the predictions. The conventional strength function is defined[18,36] as proportional to the product $a_c\bar{s}_{lj}$, where a_c is the assumed R-matrix channel radius. For s waves at very low neutron energies, this product is independent of a_c. Therefore the comparison for s waves at low energies could be made without reference to the channel radius. In fact, in the present case such a comparison could have been made for the full resonance region for s waves.[18] In general, however, such a comparison would not be valid[37] for energies of several hundred keV. The comparison for p and d waves requires[18] the boundary conditions be used consistently as done here. Another familiar quantity is the potential scattering radius R'; it is related to the s-wave external R function at zero neutron energy and is also independent of a_c. The analysis in Ref. 18 gave $R'=7.62$ fm for n-^{86}Kr. However, the values of R' determined from very low-energy scattering data have much less information than the external R functions considered here for s waves, and no corresponding information for p waves and d waves.

The remainder of this section is a more detailed evaluation of these results for the resonance region. The tops of the staircase in Fig. 5 represent the empirical sums of reduced widths for the full energy region. We see that the sum for $p_{3/2}$ is about ten times that for either s or d waves. This apparent parity dependence is related to the locations of the unoccupied single-particle states. Since the single-particle $3s$ and $2d$ states are bound fairly deeply at about -4 MeV, as shown in Fig. 3, only small fractions of their widths are found up in the resonance region. On the other hand, the single-particle $3p$ state is just unbound. Empirical evidence on the $3p$ state is provided by the well-known size resonance for the p-wave neutron strength function.[36] The resonance is centered near atomic mass $A=95$, indicating that the $3p_{1/2}$ and $3p_{3/2}$ states will become bound for masses with approximately $A>95$. For ^{86}Kr, the interactions that are represented by the imaginary part of the mean field cause a spreading of the levels such that p-wave fragments are distributed over a broad energy region extending downward into the negative energy region. It is reasonable, therefore, that a large percentage of the p-wave single-particle width is observed within the experimental region from 0 to 1 MeV. Furthermore, the fact that the cumulative sums of reduced widths in Fig. 5 is larger for $p_{3/2}$ than for $p_{1/2}$ is expected because the spin-orbit potential brings the $3p_{3/2}$ state into binding before the $3p_{1/2}$ state.

The external R functions in Fig. 4 also reflect the presence of nearby and distant single-particle states. We note from the sign of the denominator in the summation in Eq. (6.2) that the external levels lying below the experimental domain make negative contributions to R_{lj}^{ext} whereas those lying above make positive contributions. Therefore, from the preceding discussion of the energies of the single-particle states, we expect R_{lj}^{ext} to be more negative for s and d waves than for p waves. Indeed, Fig. 4 shows that to be true for both predicted and empirical values. We again caution that the values depend on the assumed channel radius; if a smaller channel radius had been assumed, all of the R_{lj}^{ext} would have been less positive but the intercomparisons would remain valid.

It is of interest to examine Fig. 5 more closely in terms of the strength functions. The slopes of the predicted curves are the strength functions, $\bar{s}_{lj}^{\text{OM}}(E)$, which are also represented by the curves in Fig. 6. We can visualize smooth curves being drawn through the empirical staircases; the slopes of these curves would be the localized empirical strength functions. Comparisons of the predicted and empirical slopes or strength functions show very good agreement except for three regions where the staircases contain excess reduced widths. These are (i) for $s_{1/2}$ for energies near 200 keV, (ii) for $p_{3/2}$ for energies near 650 keV, and (iii) for $d_{3/2}$ at 520 keV. If these concentrations were moved to outside the experimental domain, the residual staircases within the domain would be described much better by the model. Perhaps these anomalies represent doorway states.[38] The mean field should describe the interaction including doorway states, but only on the average. This suggests that the 1-MeV experimental domain may not be quite broad enough for defining the empirical averages.

The differences between the predicted and empirical $p_{3/2}$ strength functions near 650 keV are probably responsible for the differences seen in Fig. 2 between the predicted and empirical averaged total cross sections. In that figure the predictions are seen to be too low for $0.5<E<2$ MeV. This leads us to speculate that the imaginary potential might be different for p waves in this region. In this regard we note that there is little uncertainty in the Hartree-Fock potential; it has a smooth energy dependence and has been determined from analysis of a broad energy region. There is also little uncertainty in the smooth dispersive contribution resulting from the volume imaginary component. This leaves only the surface imaginary component to be adjusted. In the dispersive OMP such an adjustment is accompanied by an adjustment in the real dispersive component.

Without making the calculation, one cannot easily predict the effect on p waves of a change in the surface imag-

inary potential. Qualitatively, the strength functions are correlated with the imaginary part, and the external R functions with the real part. But there are also cross correlations. For example, an increase in the imaginary depth in the present case would spread out the p-wave distribution on both sides of the resonance region and, thereby, effect both R external and the strength function. Stated in another way, the imaginary component of the potential can affect both the off-resonance "potential" scattering and the resonance contributions.

VIII. CONCLUSIONS

The dispersive optical model potential formulated with fixed geometry and with energies referenced relative to the Fermi energy is shown to give good predictions of the n-^{86}Kr mean field over a broad energy region. The model was parametrized from empirical data on nuclei other than ^{86}Kr, except that the Fermi energy was chosen specifically for n-^{86}Kr on the basis of experimental data on the bound states. The present study does include the positive and negative energy regions that were the focus of previous dispersive optical model analyses, but the major emphasis here is on the intermediate region of resolved resonances for neutron energies up to about 1 MeV. In the resonance region the surface imaginary component is about half of the maximum value attained at higher energies, and the surface dispersive component is near its maximum. The unique feature of the present study is that it includes a more nearly complete set of empirical partial-wave scattering functions from the resonance region than any previous work and, correspondingly, more detailed comparisons with the predictions than previously. The overall success of the dispersive optical model in previous studies of other neutron-nucleus systems and for the present study of n-^{86}Kr suggest that the model can be the basis for a global model of the neutron-nucleus mean field that covers negative energies, the resonance region, and neutron energies up to at least 100 MeV.

ACKNOWLEDGMENTS

We are indebted to Dr. G. R. Satchler and Dr. C. Mahaux for helpful suggestions. Oak Ridge National Laboratory is operated by Martin Marietta Energy Systems, Inc. for the U.S. Department of Energy (DOE) under Contract No. DE-AC05-840R21400. This work was also supported by DOE Contract Nos. DE-FG02-87ER40326 and DE-FG05-86ER40293 with Denison University and Middle Tennessee State University, respectively.

[1]C. Mahaux and H. Ngô, Nucl. Phys. **A378**, 205 (1982).
[2]C. Mahaux and R. Sartor, Nucl. Phys. **A468**, 193 (1987).
[3]C. Mahaux and R. Sartor, Nucl. Phys. **A475**, 247 (1987).
[4]C. Mahaux and R. Sartor, Nucl. Phys. **A481**, 381 (1988).
[5]C. Mahaux and R. Sartor, Nucl. Phys. **A484**, 205 (1988).
[6]C. H. Johnson, D. J. Horen, and C. Mahaux, Phys. Rev. C **36**, 2252 (1987).
[7]C. H. Johnson and C. Mahaux, Phys. Rev. C **38**, 2589 (1988).
[8]C. Mahaux and R. Sartor, Phys. Rev. C **36**, 1777 (1987).
[9]J. P. Delaroche, Y. Wang, and J. Rapaport (unpublished).
[10]R. D. Lawson, P. T. Guenther, and A. B. Smith, Phys. Rev. **34**, 1599 (1986).
[11]R. L. Walter and P. P. Guss, in *Nuclear Data for Basic and Applied Science,* edited by P. G. Young, R. E. Brown, G. F. Auchampaugh, P. W. Lisowski, and L. Stewart (Gordon and Breach, New York, 1986), Vol. 2, p. 1079.
[12]G. M. Honoré, R. S. Pedroni, C. R. Howell, H. G. Pfutzner, R. C. Byrd, G. Tungate, and R. L. Walter, Phys. Rev. C **34**, 825 (1986).
[13]A. M. Lane and R. G. Thomas, Rev. Mod. Phys. **30**, 257 (1958).
[14]C. H. Johnson, N. M. Larson, C. Mahaux, and R. R. Winters, Phys. Rev. C **27**, 1913 (1983).
[15]C. H. Johnson, C. Mahaux, and R. R. Winters, Phys. Rev. C **32**, 359 (1985).
[16]D. J. Horen, C. H. Johnson, and A. D. MacKellar, Phys. Lett. **161B**, 217 (1985).
[17]D. J. Horen, C. H. Johnson, J. L. Fowler, A. D. MacKellar, and B. Castel, Phys. Rev. C **34**, 429 (1986).
[18]R. F. Carlton, R. R. Winters, C. H. Johnson, N. W. Hill, and J. A. Harvey, Phys. Rev. C **38**, 1605 (1988).
[19]Y. Wang and J. Rapaport, Nucl. Phys. **A454**, 359 (1986).
[20]J. R. M. Annand, R. W. Finlay, and F. S. Dietrich, Nucl. Phys. **A443**, 249 (1985).
[21]A. B. Smith, P. T. Guenther, and R. D. Lawson, Nucl. Phys. **A455**, 344 (1986).
[22]J.-P. Jeukenne, C. H. Johnson, and C. Mahaux, Phys. Rev. C **38**, 2573 (1988).
[23]C. H. Johnson and R. R. Winters, Phys. Rev. C **37**, 2340 (1988).
[24]G. E. Brown and M. Rho, Nucl. Phys. **A271**, 397 (1981).
[25]J. Rapaport, Phys. Rep. **87**, 25 (1982).
[26]P. Luksch and J. W. Tepel, Nucl. Data Sheets **27**, 389 (1979).
[27]K. Haravu, C. L. Hollas, P. J. Riley, and W. R. Coker, Phys. Rev. C **1**, 938 (1970).
[28]N. A. Detorie, P. L. Jolivette, C. P. Browne, and A. A. Rollefson, Phys. Rev. **18**, 991 (1978).
[29]B. Rosner and E. J. Schneid, Nucl. Phys. **82**, 182 (1966).
[30]C. M. Fou and R. W. Zurmühle, Phys. Rev. **176**, 1339 (1968).
[31]J. W. Tepel, Nucl. Data Sheets **30**, 501 (1980).
[32]C. Mahaux, P. F. Bortignon, R. A. Broglia, and C. H. Dasso, Phys. Rep. **120**, 1 (1985).
[33]C. H. Johnson and R. R. Winters, Phys. Rev. C **27**, 416 (1983).
[34]R. R. Winters, C. H. Johnson, and A. D. MacKellar, Phys. Rev. C **31**, 384 (1985).
[35]C. H. Johnson and R. R. Winters, Phys. Rev. C **21**, 2190 (1980).
[36]S. F. Mughabghab, M. Divadeenam, and N. S. Holden, *Neutron Cross Sections* (Academic, New York, 1981), Vol. 1.
[37]C. H. Johnson, in *Neutron-Nucleus Collisions a Probe of Nuclear Structure,* edited by J. Rapaport, R. W. Finlay, S. M. Grimes, and F. S. Dietrich (AIP, New York, 1985), p. 446.
[38]B. Block and H. Feshbach, Ann. Phys. (N.Y.) **23**, 47 (1963).